IEEE Access
Multidisciplinary | Rapid Review | Open Access Journal

Received January 4, 2021, accepted January 25, 2021, date of publication February 5, 2021, date of current version February 12, 2021.

Digital Object Identifier 10.1109/ACCESS.2021.3057489

Nonlocal Low-Rank and Prior Image-Based Reconstruction in a Wavelet Tight Frame Using Limited-Angle Projection Data

NA XU[1], HUILING HOU[1], ZHIYONG CHENG[1], MINGQUAN WANG[1], YU WANG[1], AND GUOGANG WANG[2]

[1]College of Information and Communication Engineering, North University of China, Taiyuan 030051, China
[2]College of Physical and Electronic Engineering, Shanxi University, Taiyuan 030006, China

Corresponding author: Mingquan Wang (wangmq@nuc.edu.cn)

This work was supported in part by the National Special Project for the Development of Major Scientific Instruments and Equipment of China under Grant 2013YQ240803, in part by the Scientific Research Foundation of North China University under Grant XJJ2016023, in part by the Shanxi Province Universities Science and Technology Innovation Project under Grant 2017107, and in part by the Natural Science Foundation of Shanxi Province under Grant 201901D111031.

ABSTRACT Computed tomography (CT) reconstruction for limited-angle projection data is an ill-posed inverse problem, that often produces artifacts near the edges of an image. In this study, a hybrid minimization model based on a nonlocal low-rank approximation and a prior image in a wavelet tight framework is proposed to improve reconstructions from limited-angle projections. Low-frequency wavelet coefficients of the reconstructed image were estimated using a nonlocal low-rank approximation and the l_2 norm minimization was applied to the difference between the high-frequency components of a prior image and the reconstructed image. In addition, the alternative direction method of multipliers (ADMM) was used for alternately minimization to solve two regularization terms which produce the most parameters. Experimental results demonstrated that the proposed algorithm offers several advantages over conventional iterative reconstruction techniques, including faster convergence, suppression of limited-angle artifacts, noise reduction, and the preservation of edges and other image details. This study represents the first time that nonlocal low-rank prior information has been applied to limited-angle CT.

INDEX TERMS Computed tomography (CT), limited-angle projections, low-rank approximation, prior image, wavelet tight frame.

I. INTRODUCTION

Computed tomography (CT) with under-sampled projection data has attracted increased attention in recent years. The problem is generally ill-posed and includes both sparse projections, acquired by scanning an object at equal intervals in the range of [0, 360°], and limited-angle data collected over restricted viewing angles (typically less than 180°). Improving sparse tomography algorithms is of critical importance as restricted scanning conditions are common in a variety of practical applications [1], [2]. For example, industrial nondestructive testing involves the use of CT to detect defects in service pipelines [3], large target objects [4], cylindrical structures [5], and other wide-angle fields for which only limited-angle projections can be acquired [6]. An example of a limited scanning geometry is shown in Fig. 1. In these configurations, the filtered back projection (FBP) [7] algorithm used in commercial CT (as well as other conventional techniques [8]–[10]) does not work well because the projection data are incomplete. This often produces artifacts near the edges of a reconstructed image, as shown in Fig. 2.

The reconstruction of limited-angle projections requires an understanding of limited-angle CT algorithms. This process can be represented as determining an attenuation coefficient X (a CT image) from incomplete projection data corrupted by noise:

$$p = AX + \xi \tag{1}$$

where $\xi \in \mathrm{R}^M$ denotes the noise, $p \in \mathrm{R}^M$ is the projection vector, $X \in \mathrm{R}^N$ is the image to be reconstructed, and

The associate editor coordinating the review of this manuscript and approving it for publication was Ravibabu Mulaveesala.

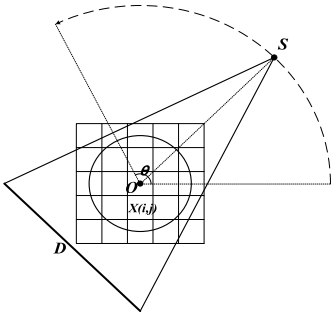

FIGURE 1. Limited-angle CT scanning geometry. Here, *S* denotes the X-ray source, *O* is the object rotation center, *D* is the detector, θ is a rotation angle (<180°), and *X*(*i*,*j*) represents the reconstructed image pixel value at the position (*i*,*j*).

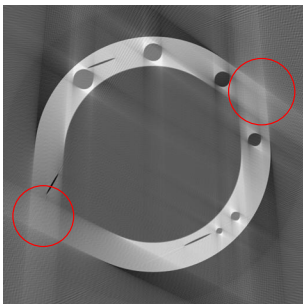

FIGURE 2. Reconstructed results from a simulation phantom that includes two small porosities and three cracks, using the FBP algorithm at a scanning angle of [0, 120°]. Limited-angle artifacts are marked by the red circles.

$A \in \mathrm{R}^{M\times N}$ ($M \ll N$) denotes a system matrix for the X-ray transform.

Since the limited-angle projection data are seriously incomplete, the reconstruction problem is ill-posed, and regularization must be included to stabilize the procedure of limited-angle reconstruction. This regularization term includes a priori information concerning the solution and must be included in the reconstruction process. In this study, the Tikhonov algorithm was applied, in which a regularized solution X_μ was acquired in the following optimization problem:

$$X_\mu \in \arg\min_{X\in\psi}\{\frac{1}{2}\|AX-p\|_2^2+\mu F(X)\} \tag{2}$$

where ψ denotes a convex set, $\mu > 0$ is a regularization parameter, and F: $\psi \rightarrow[0, +\infty]$ is a regularization (or penalty) function (that may be either convex or non-convex). The term $\|AX-p\|_2^2$ is a data fidelity term that controls error and $F(X)$ is the penalty term or prior term that includes prior knowledge of the object.

The primary objective of CT image reconstruction is to generate high-resolution images or keep the special edges through the selection of regularization functions. This can be accomplished using various control metrics including the total variation (TV) norm, which is used to preserve edges and can be expressed as [11]–[13]:

$$\|X\|_{TV}=\sum_{i,j}\sqrt{(X_{i,j}-X_{i-1,j})^2+(X_{i,j}-X_{i,j-1})^2} \tag{3}$$

Regularization parameters of this type have been applied during various phases of reconstruction in previous studies. For example, Sidky *et al.* considered the sparsity of images produced with a gradient transform and proposed the projection of convex sets total variation minimization (POCS-TVM) algorithm, which can be expressed as [14]:

$$\min\|X\|_{TV} \quad s.t.\,, X\geq 0 \tag{4}$$

In addition, projection data used in the practical limited-angle reconstructions typically include noise. Thus, Eq. (4) can be rewritten as:

$$\min\|X\|_{TV} \quad s.t.\ \|AX-p\|_2^2\leq\delta^2,\ X\geq 0 \tag{5}$$

where δ denotes the noise level.

High-quality reconstructions can be produced using the POCS-TVM algorithm for sparse-view sampling implemented over a range of 360°. However, TV-based models struggle to suppress edge artifacts or distortions in images when the scanning angle is restricted [15], [16]. As such, variations of TV-based models have been proposed to overcome this limitation. One approach includes alternate minimization in the limited-angle reconstruction problem. For example, Lu *et al.* developed a new alternating optimization technique for limited-angle reconstruction problems by combining a gradient with the TV-norm [17]. Another approach involves improving the TV algorithm in an iterative process. Lu *et al.* proposed a novel iterative regularization algorithm in which a data error term was used as the weight of a TV term, to form a new objective function and improve limited-angle reconstructions [18]. Chen *et al.* proposed the use of an anisotropic TV norm (ATV norm) for minimizing image sparsity and reducing the imbalance between TV minimization and anisotropic data fidelity constraints, due to incomplete projections [15]. These techniques reduced limited-angle artifacts near the edges of the reconstructed image, but edge distortion remained an issue.

TV models assume images to be piecewise constant, which may degrade relevant pixel information [19]. For example, Kumar and Shneider demonstrated the strong structural similarity between different image patches and showed that matrices composed of similar patches exhibit low-rank features [20]. Dong *et al.* first introduced nonlocal low-rank regularization into image reconstruction by exploiting nonlocal self-similarity and group sparsity [21]. Sagheer *et al.* used a nonlocal low-rank approximation and a TV model to describe the global correlation and local smoothness of an image, respectively. This technique preserved image details and reduced noise in denoising of low-dose CT images [22]. Motivated by this approach, this study introduces nonlocal low-rank regularization into the reconstruction process for limited-angle CT, to suppress limited-angle artifacts.

Over the past decade, wavelet frame-based algorithms have been used for sparse-view CT image reconstruction [23]–[26]. The basic theory is that reconstructed images can be sparsely approximated by wavelet coefficients in a suitable tight wavelet frame. The corresponding unconstrained optimization problem can then be expressed as:

$$\min_{X\in\psi} \frac{1}{2} \|AX - p\|_2^2 + \alpha \|WX\|_b \tag{6}$$

where ψ is a convex set, $\alpha > 0$ is a regularization parameter, W denotes a wavelet frame, and b = 0 and b = 1 denote the l_0 and l_1 norms, respectively. High-quality reconstructions can then be produced from sparse-view projections. However, in the case that the scanning range is severely limited, limited-angle artifacts will typically occur near the edges of reconstructed images.

Some studies have attempted to overcome sparse data issues by integrating a prior image into the reconstruction process. For example, Chen *et al.* introduced the prior image constrained compressed sensing (PICCS) algorithm, in which each frame of a prior CT image sequence was reconstructed using projections from sparse dynamic data [27]. PICCS algorithm has been further used to improve the temporal resolution of cardiac CT [28], [29] and the image quality for CT dose reduction [30], [31]. The PICCS algorithm can be expressed as [27], [32]:

$$X_\alpha \in \arg\min\{\alpha \|D_1(X - X_0)\|_1 + (1\text{-}\alpha) \|D_2X\|_1\}, \quad s.t\ AX = p \tag{7}$$

where D_1 and D_2 denote discrete gradient transforms, X_0 represents a prior image, and $\alpha > 0$ is a regularization parameter. PICCS also includes the algebraic reconstruction technique (ART), which can be used to estimate an image X by iteratively bringing its current projection data (AX) closer to measured values (p). The standard steepest descent algorithm was then used to minimize the weighted summation of the total variation. This process can effectively preserve edges in a reconstructed sparse-view CT image when parameters are chosen properly.

Nondestructive evaluation can also be performed using a prior image, obtained from full-scan data, in combination with the FBP or POCS-TVM algorithms. For example, pipelines are often fixed to a wall or floor and can only be scanned from a limited angular range due to the restricted geometry. However, follow-up detection can be performed with a prior image acquired from full-scan data before the pipeline was installed. The resulting limited-angle reconstruction of the pipeline in service will be very close to the prior image. The corresponding differences represent abnormalities, such as cracks, that can be used to identify problems.

This study proposes a new model based on a nonlocal low-rank approximation, and a prior image acquired under a wavelet tight framework, for limited-angle CT reconstruction. This algorithm is able to suppress artifacts near the borders of an image while preserving edges. The associated objective function includes two regularization terms and a data fidelity term. One of the regularization terms is based on a nonlocal low-rank approximation that exploits nonlocal self-similarity and group sparsity in a wavelet tight frame. The other represents the difference between the high-frequency component of the prior image and the reconstructed image. A nonlocal low-rank approximation was used to suppress limited-angle artifacts by restricting small low-frequency wavelet coefficients. Unlike the PICCS algorithm, in which prior image information is used for reconstruction, the proposed technique preserves edges by minimizing only the l_2 norm of the differences between the high-frequency components of the prior and reconstructed images. In addition, since regularization terms introduce more parameters, the alternative direction method of multipliers (ADMM) [33] was used to alternately solve the minimization problem. Experimental results showed the proposed algorithm successfully suppressed limited-angle artifacts and noise while preserving edges in limited-angle CT reconstructions.

The remainder of this paper is organized as follows. The wavelet tight frame and the nonlocal low-rank approximation are introduced in Section II. The proposed reconstruction model is derived and numerically solved in Section III. Representative experiments are designed, and corresponding results are analyzed, in Section IV. Finally, conclusions are provided in Section V.

II. BASIC THEORY

A. THE WAVELET TIGHT FRAME

In this subsection, the wavelet tight frame is introduced as follows. Let $\{b_n\}_{n\in N}$ denote a sequence in the Hilbert space H, where N is a countable set. If two constants ($0<A<+\infty$ and $0<B<+\infty$) exist, such that:

$$A\|\boldsymbol{a}\|^2 \le \sum_{n\in N} |\langle \boldsymbol{a}, \boldsymbol{b_n}\rangle|^2 \le B\|\boldsymbol{a}\|^2 \quad (\forall \boldsymbol{a} \in H) \tag{8}$$

then the sequence $\{b_n\}_{n\in N}$ represents a frame for H. The two constants (A and B) are then the lower and upper bounds of the frame $\{b_n\}_{n\in N}$, respectively. If $A = B$, the frame $\{b_n\}_{n\in N}$ is a tight frame for H and can be expressed as:

$$\|\boldsymbol{a}\|^2 = \sum_{n\in N} |\langle \boldsymbol{a}, \boldsymbol{b_n}\rangle|^2 \quad (\forall \boldsymbol{a} \in H) \tag{9}$$

Tight frames include two associated operators. One is the analysis operator W, defined as:

$$W : \boldsymbol{a} \in H \to \{\langle \boldsymbol{a}, b_n\rangle\} \in \ell_2(N) \tag{10}$$

in which the sequence $\langle \boldsymbol{a}, b_n\rangle$ is a canonical frame coefficient sequence. The other is a synthesis operator W^T given by:

$$W^T : \{a_n\} \in \ell_2(N) \to \sum_{n\in N} a_n b_n \in H \tag{11}$$

The unitary extension principle states that since $W^TW = I$ in the tight frame, I is an identity operator. Any image X can then be represented by $X = W^T WX$.

A general flowchart for two-dimensional discrete wavelet transforms (2D-DWT) is shown in Fig. 3. The 2D image

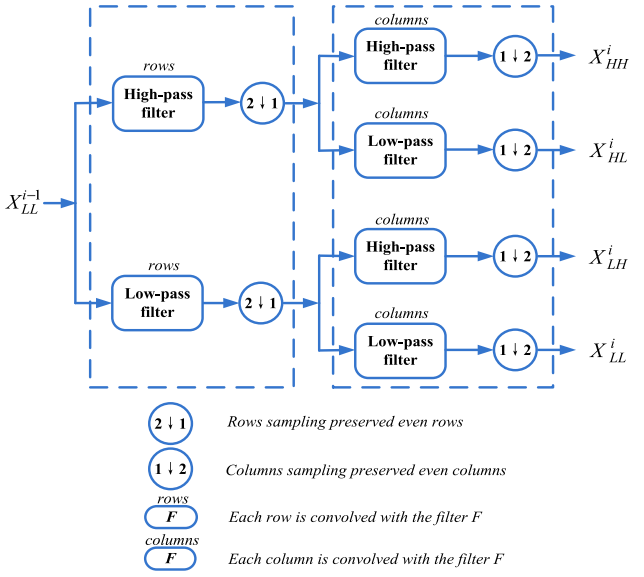

FIGURE 3. A flowchart of the two-dimensional discrete wavelet transform (2D-DWT).

was first filtered in the horizontal direction (rows) to obtain low-frequency (L) and high-frequency (H) sub-bands; these sub-bands (L and H) were then filtered further in the vertical direction (columns) to produce low-frequency (LL), horizontal high-frequency (LH), vertical high-frequency (HL), and diagonal high-frequency (HH) sub-bands.

Assuming the input image is given by X^0, k represents the order of the wavelet decomposition expressed as:

$$\begin{aligned}[X^1_{LL}, X^1_{LH}, X^1_{HL}, X^1_{HH}] &= WX^0 \\ [X^2_{LL}, X^2_{LH}, X^2_{HL}, X^2_{HH}] &= WX^1_{LL} \\ &\text{M} \\ [X^k_{LL}, X^k_{LH}, X^k_{HL}, X^k_{HH}] &= WX^{k-1}_{LL}\end{aligned} \tag{12}$$

Wavelet reconstruction can be performed in a similar manner [34], [35].

B. NONLOCAL LOW-RANK REGULARIZATION

The nonlocal low-rank regularization model is based on a basic assumption that self-similarity is abundant in the signals of interest [21], [36]. This assumption implies that a sufficient number of similar patches can be found for any exemplar patch of size $\sqrt{n} \times \sqrt{n}$ at position j, denoted by $x_j \in \mathrm{R}^n$. Let $X_j = [R_{j_0}x, R_{j_1}x, \ldots, R_{j_{m-1}}x] \in \mathrm{R}^{n\times m}$ denote a data matrix composed of a set of image patches similar to x_j (including x_j itself). This set of similar patches can then be formed using a block matching technique in which the m patches closest to x_j (including x_j itself) are selected using a k-nearest-neighbor search method in a local window (e.g., 40×40).

Under the assumption that these image patches exhibit similar structure, the resulting data matrix X_j will be of low-rank. In practice, the data X_j may be corrupted by noise and can thus be modeled as $X_j = L_j + N_j$, where L_j and N_j denote the low-rank and the Gaussian noise components, respectively. The low-rank matrix L_j can then be estimated by solving the following optimization problem:

$$L_j = \arg\min_{L_j} rank(L_j), \qquad s.t.\ \left\|X_j - L_j\right\|_F^2 \le \delta_\omega^2 \tag{13}$$

where $\|\cdot\|_F^2$ denotes the Frobenious norm and δ_ω^2 represents the variance of additive Gaussian noise. Since the rank operator is non-convex and non-continuous, rank-minimization is an NP-hard problem. The nuclear norm $||\cdot||_*$ is often used as a convex surrogate of rank$(\cdot)$. However, in this study, a smooth but nonconvex surrogate of the rank was used to improve performance. Specifically, the logdet$(\cdot\ )$ function given by [37]

$$\begin{aligned}L(L_j, \varepsilon) &= \log\det((L_jL_j^T)^{1/2} + \varepsilon I) \\ &= \log\det(\Lambda^{1/2} + \varepsilon I) \\ &= \sum_{r=1}^{r_0} \log(\sigma_r(L_j) + \varepsilon)\end{aligned} \tag{14}$$

was included as a nonconvex surrogate. Here, ε is a small constant, $L_j \in R^{n\times m}$ and Λ is a diagonal matrix whose non-zero elements are eigenvalues of the matrix $L_jL_j^T$. In addition, $L_jL_j^T = U\Lambda U^{-1}$, where $\Lambda^{1/2}$ is a diagonal matrix whose non-zero elements are the singular values of the matrix L_j. The term $\sigma_r(L_j)$ denotes the r^{th} singular value of L_j and $r_0 = \min(n, m)$. Dong *et al.* demonstrated that the logdet$(\cdot)$ function offers better performance than the nuclear norm in low-rank approximations [21]. The optimization problem represented by (8) can then be rewritten as:

$$L_j \in \arg\min_{L_j} \left\|X_j - L_j\right\|_F^2 + \lambda L(L_j, \varepsilon) \tag{15}$$

where λ is a Lagrange multiplier. The matrix X_j can be approximated with a low-rank matrix L_j in any exemplar patch, by solving (15). The low-rank matrix L_j can further enforce low-rank properties for each extracted exemplar image patch, over a set of nonlocal similar patches. The global objective functional based on nonlocal low-rank regularization can then be written as:

$$X \in \arg\min_{X, L_j} \|AX - p\|_2^2 + \eta \sum_j \{\left\|\tilde{R}_j x - L_j\right\|_F^2 + \lambda L(L_j, \varepsilon)\} \tag{16}$$

where $\tilde{R}_j x = [R_{j1}x, R_{j2}x, \ldots, R_{jm}x]$ denotes a data matrix composed of data selected from the set of image patches similar to x_j. Nonlocal low-rank regularization can exploit both the group sparsity of similar patches and the nonconvexity of rank minimization, thus achieving better performance than nuclear norm for low-rank approximations [21].

III. PROPOSED RECONSTRUCTION MODEL AND NUMERICAL ALGORITHM

In this section, a novel reconstruction model is proposed for solving the limited-angle problem, which is based on a nonlocal low-rank approximation and a prior image under a proper

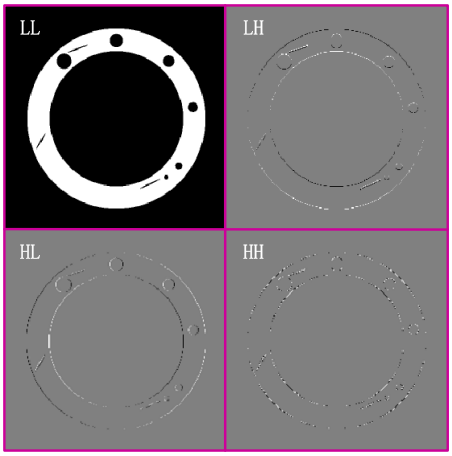

FIGURE 4. Wavelet transform results for the original phantom in a Haar wavelet tight frame.

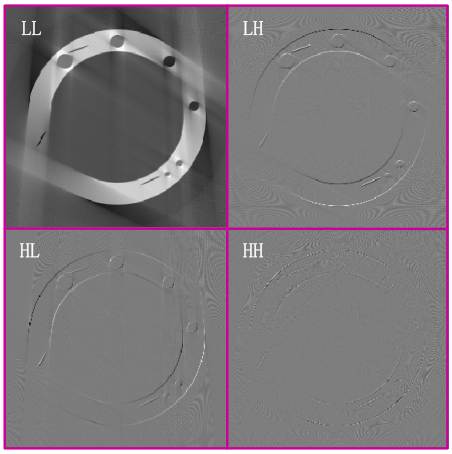

FIGURE 5. Wavelet transform results for Fig. 2 in a Haar wavelet tight frame.

wavelet tight frame. An efficient alternative minimization technique is also presented for the proposed reconstruction algorithm.

A. PROPOSED RECONSTRUCTION MODEL

Limited-angle reconstructions often include artifacts caused by the incompleteness of projection data (see Fig. 2). To address this problem, a prior image similar to the estimated solution was embedded into the reconstruction model. It has also been shown that reconstructed images can be accurately approximated by sparse coefficients under a proper wavelet tight frame. In this paper, the Haar wavelet was used for 2D discrete wavelet transforms. The scale function was [1, 1] and the wavelet function was [1, −1].

The original phantom, the image reconstructed using the FBP algorithm (for the scanning range [0, 120°]), and the 1-level wavelet decomposition are shown in Figs. 4 and 5. The LL sub-band includes the low-frequency coefficients, while the LH, HL, and HH sub-bands contain high-frequency coefficients. As seen in the figures, the low-frequency wavelet coefficients were degraded, and their sparsity in the reconstructed images exhibiting limited-angle artifacts was lower than that of the original phantom. To solve this problem, a nonlocal low-rank approximation regularization term was included to penalize smaller low-frequency wavelet coefficients in reconstructed images and ensure their sparsity. The edges of the reconstructed image were also distorted, which corresponds to high-frequency wavelet coefficients. This effect was corrected by exploiting a similar (prior) image obtained in advance. The high-frequency components of the estimated image, which is very close to the original phantom, can then be used as prior information in minimizing the l_2 norm of the difference between the high-frequency component of the prior image and that of the reconstructed image. This approach produced high frequency components (in the reconstructed image) that were closer to those of the prior image, thereby preserving edges in limited-angle reconstructions. In addition, the noise present in these high-frequency components can be effectively suppressed by minimizing the l_2 norm.

Thus, both the sparsity of low-frequency wavelet coefficients and high-frequency information in the prior image can be used to suppress limited-angle artifacts and noise, thereby preserving edges and improving image quality. The following minimization model is proposed to improve limited-angle reconstructions:

$$\begin{aligned} &\arg\min_{X\in\psi}\{\frac{\mu}{2}\|(WX)_H-(WX_0)_H\|_2^2+\tau NLR((WX)_L)\},\\ &s.t.\ \ \|AX-p\|_2^2\le\delta^2 \end{aligned} \tag{17}$$

where $WX=((WX)_L,(WX)_H)$, X_0 is a prior image, X denotes the reconstructed image estimation, $\psi=\{X\in\mathrm{R}^N\ |X>0\}$ denotes a convex set, $(WX)_H$ and $(WX_0)_H$ denote the high-frequency components of wavelet coefficients for the images X and X_0, $(WX)_L$ denotes the low-frequency components of X, $NLR(\cdot)$ is a nonlocal low-rank approximation term, $p\in\mathrm{R}^M$ represents the projection data, $A\in\mathrm{R}^{M\times N}(M\ll N)$ is the X-ray transform matrix for limited-angle data and μ and τ are positive regularization parameters. The $NLR(\cdot)$ term is given by:

$$\begin{aligned} &NLR((WX)_L)\\ &=\sum_j\{\left\|\tilde{R}_j(WX)_L-L_j\right\|_F^2+\lambda L(L_j,\varepsilon)\}\\ &=\sum_j\{\left\|\tilde{R}_j(WX)_L-L_j\right\|_F^2+\lambda\sum_{r=1}^{r_0}\log(\sigma_r(L_j)+\varepsilon)\} \end{aligned} \tag{18}$$

B. NUMERICAL ALGORITHM

The objective function in (17) must be alternately implemented in image domain space and wavelet domain space, which inevitably complicates the solution. However, this problem can be converted into two sub-problems solved iteratively and alternately, as shown below [38]:

$$\text{Sub-problem1}:\arg\min_{X\ge0}\|AX-p\|_2^2\le\delta^2 \tag{19}$$

$$\text{Sub-problem2}: \arg\min_{X\geq 0} \frac{1}{2}\left\|X-\hat{X}\right\|_2^2 + \tau NLR((WX)_L) + \frac{\mu}{2}\|(WX)_H - (WX_0)_H\|_2^2 \quad (20)$$

In sub-problem 1, the estimated image $\hat{X}$ can be acquired using the simultaneous algebraic reconstruction technique (SART) to ensure data fidelity. In sub-problem 2, two regularization terms are utilized to further improve the estimated image $\hat{X}$. An auxiliary variable $Z = WX$ was also included in the wavelet domain as $Z = (Z_L, Z_H)$. Equation (20) is then equivalent to the following minimization problem:

$$\arg\min_{X\geq 0} \frac{1}{2}\left\|X-\hat{X}\right\|_2^2 + \tau NLR(Z_L) + \frac{\mu}{2}\|Z_H - (WX_0)\|_2^2 \quad s.t.\ WX = Z \quad (21)$$

The augmented Lagrange method can be used to convert (21) into the following unconstrained optimization model:

$$\arg\min_{X\geq 0,Z} \frac{1}{2}\left\|X-\hat{X}\right\|_2^2 + \tau NLR(Z_L) + \frac{\mu}{2}\|Z_H - (WX_0)_H\|_2^2 + y^T(WX-Z) + \frac{\rho}{2}\|WX-Z\|_2^2 \quad (22)$$

where ρ is a penalty parameter and y is a dual variable. Setting $u = (1/\rho)y$ and $v = WX\text{-}Z$ produces the following:

$$y^T v + \frac{\rho}{2}\|v\|_2^2 = \frac{\rho}{2}\left\|v+\frac{1}{\rho}y\right\|_2^2 - \frac{1}{2\rho}\|y\|_2^2 = \frac{\rho}{2}\|v+u\|_2^2 - \frac{\rho}{2}\|u\|_2^2 \quad (23)$$

where $\frac{\rho}{2}\|u\|_2^2$ is a constant term that does not affect the location of the minimal solution and can be ignored. When this expression is introduced into (22), the optimization model can be represented as:

$$\arg\min_{X\geq 0,Z,u} \frac{1}{2}\left\|X-\hat{X}\right\|_2^2 + \tau NLR(Z_L) + \frac{\mu}{2}\|Z_H - (WX_0)_H\|_2^2 + \frac{\rho}{2}\|WX-Z+u\|_2^2 \quad (24)$$

The solution of this optimization problem was identified using the ADMM algorithm to separate the variables X, Z, and u, generating three sub-problems corresponding to each variable. An approximate expression for the $k+1$ iteration of this alternately minimized sub-problem is given by:

$$X^{k+1} \in \arg\min_{X^k\geq 0} \frac{1}{2}\left\|X^k-\hat{X}\right\|_2^2 + \frac{\rho}{2}\left\|WX^k - Z^k + u^k\right\|_2^2; \quad (24\text{-a})$$

$$Z^{k+1} \in \arg\min_{Z^k} \frac{\mu}{2}\left\|Z_H^k - (WX_0)_H\right\|_2^2 + \tau NLR(Z_L^k) + \frac{\rho}{2}\left\|WX^{k+1} - Z^k + u^k\right\|_2^2 \quad (24\text{-b})$$

$$u^{k+1} = u^k - (WX^{k+1} - Z^{k+1}). \quad (24\text{-c})$$

A closed solution to sub-problem (24-a) can be acquired by finding derivatives of X and setting them to zero:

$$X^{k+1} = \max\left(\frac{\hat{X} + \rho W^T(Z^k - u^k)}{1+\rho}, 0\right) \quad (25)$$

where W^T denotes a reconstruction operator for the Haar wavelet transform.

In sub-problem (24-b), $\frac{\rho}{2}\|(WX)_H - Z_H + u_H\|_2^2 + \frac{\rho}{2}\|(WX)_L - Z_L + u_L\|_2^2 = \frac{\rho}{2}\|WX - Z + u\|_2^2$ such that the low-freque-ncy (Z_L) and high-frequency (Z_H) components of the wavelet coefficients Z are solved separately. The sub-problem (24-b) can then be divided into two minimization problems:

Low frequency:

$$Z_L^{k+1} \in \arg\min_{Z_L^k}\{\tau NLR(Z_L^k) + \frac{\rho}{2}\left\|(WX^{k+1})_L - Z_L^k + u_L^k\right\|_2^2\} \quad (26)$$

High frequency:

$$Z_H^{k+1} \in \arg\min_{Z_H^k}\{\frac{\mu}{2}\left\|Z_H^k - (WX_0)_H\right\|_2^2 + \frac{\rho}{2}\left\|(WX^{k+1})_H - Z_H^k + u_H^k\right\|_2^2\} \quad (27)$$

Equation (26) can then be expanded as follows:

$$Z_L^{k+1} \in \arg\min_{Z_L^k} \tau\sum_j\{\left\|\tilde{R}_j Z_L^k - L_j\right\|_F^2 + \lambda L(L_j,\varepsilon)\} + \frac{\rho}{2}\left\|(WX^{k+1})_L - Z_L^k + u_L^k\right\|_2^2 \quad (28)$$

where $L_j^{k+1} = \arg\min_{L_j}\left\|\tilde{R}_j Z_L^k - L_j\right\|_F^2 + \lambda L(L_j,\varepsilon)$ can be optimized to obtain a low-rank matrix using the weighted singular value threshold method [21]. In other words, low-rank optimization is conducted for each exemplar image patch of the low-frequency coefficient Z_L. The corresponding expression of the low-rank approximate solution for similar patch groups is given by:

$$L_j^{k+1} = U(\tilde{\Lambda} - \frac{\lambda}{2\tau}diag(\boldsymbol{\omega}^k))_+ V^T \quad (29)$$

where $U\tilde{\Lambda}V^T$ is the singular value decomposition (SVD) of the similar patch group X_j ($X_j = \tilde{R}_j Z_L$), $\omega_r^k = 1/(\delta_r^k + \varepsilon)$ are the weights in an ascending order (the singular value $\delta_r(L_j^k)$ is in descending order), and $(x)_+ = \max\{x, 0\}$.

After solving for each L_j, the expression in (28) is equivalent to the following optimization problem:

$$Z_L^{k+1} \in \arg\min_{Z_L^k} \tau\sum_j\left\|\tilde{R}_j Z_L^k - L_j\right\|_F^2 + \frac{\rho}{2}\left\|(WX^{k+1})_L - Z_L^k + u_L^k\right\|_2^2 \quad (30)$$

A closed form solution of Z_L^{k+1} can be obtained for fixed X^{k+1} and u_L^k as follows:

$$Z_L^{k+1} = (\tau \sum_j \tilde{R}_j^T \tilde{R}_j + \frac{\rho}{2} I)^{-1} (\frac{\rho}{2}((WX^{k+1})_L + u_L^k) + \tau \sum_j \tilde{R}_j L_j) \quad (31)$$

where the term $\sum_j \tilde{R}_j^T \tilde{R}_j$ is a diagonal matrix in which each element corresponds to an image pixel position whose value is the number of overlapping patches covering the pixel location. The term $\sum_j \tilde{R}_j L_j$ denotes the average result of collected similar patches for each exemplar patch.

An approximate solution of (27) can be acquired using first-order optimization condition as follows:

$$Z_H^{k+1} = \frac{\mu(WX_0)_H + \rho((WX^{k+1})_H + u_H^k)}{\mu + \rho} \quad (32)$$

where, $Z^{k+1} = (Z_L^{k+1}, Z_H^{k+1})$.

The process of iterative minimization with respect to X, Z, and u is summarized as pseudo code below. Here, K_{iter} denotes the maximum number of iterations and α is a relaxation factor in the SART algorithm, which controls the iteration step-size. The implementation of iterative minimization for the CT reconstruction model proposed in this paper is presented below:

Proposed Algorithm

Initialization: α, ρ, τ, μ, λ, $X^1 = 0$, $Z^1 = WX^1$, K_{iter}, $k = 1$.

For k = 1 to K_{iter} do:

(1) Update $\hat{X}$ using SART:

$$\hat{X}_j^{k+1} = X_j^k + \alpha \frac{\sum \frac{p_m - \sum_{j=1}^{N} a_{mj} X_j^k}{\sum_{j=1}^{N} a_{mj}^2} a_{mj}}{\sum_{p_m \in p} a_{mj}} \quad \begin{matrix} m = 1, 2, \ldots, M \\ j = 1, 2, \ldots, N \end{matrix}$$

Positivity constraint $\hat{X}_j^{k+1} = \begin{cases} \hat{X}_j^{k+1}, \hat{X}_j^{k+1} \geq 0 \\ 0, \quad \hat{X}_j^{k+1} < 0 \end{cases}$.

(2) Update X:

Determine X^{k+1} using (25).

(3) Update Z:

Solve for Z^{k+1} in (30) and (31).

(4) Update u:

Obtain u^{k+1} using (24-c).

end

Output $X^{K_{iter}}$.

IV. NUMERICAL VALIDATION

Two experiments were conducted, using simulated and measured data, to verify the performance of the algorithm developed in this study for limited-angle CT reconstruction. The proposed technique was compared with SART, POCS-TVM, PICCS, and the FBP model. The resulting performance was evaluated in terms of the number of different scanning angles, the stability of noise projections, CT reconstruction quality, and convergence speed. All experiments were conducted on a 3.40 GHz Intel(R) Core (TM) i5-7500 CPU processor with 8 GB memory.

The influence of certain factors, such as noise level, reconstructed objects and projection data make it difficult to optimize parameters and iteration numbers during CT reconstruction. As such, these values were selected using trial and error. In addition, the quantitative performance of each algorithm was assessed using the root mean square error (RMSE) [39], peak signal-to-noise ratio (PSNR) [40], and mean structural similarity index (MSSIM) [41].

A. EXPERIMENT ON SIMULATED DATA WITH MIXED POISSON-GAUSSIAN NOISE

The proposed algorithm was validated using a simulated phantom containing two small porosities of different sizes and three cracks in different directions (not included in the prior image), as shown in Fig. 6. Geometric scanning parameters for the simulated limited-angle CT reconstruction system are listed in Table. 1. Projections were acquired by selecting scanning ranges of [0, 120°], [0, 100°], and [0, 80°] with 1° increments.

Measurement noise is inevitable in practical applications. Thus, a mixed-noise model was included to more accurately verify the stability of the proposed algorithm. Two noise sources were added to the projection data (quantum X-ray noise and electronic noise) to represent Poisson [42] and Gaussian distributions [43], respectively. This approach was used to effectively evaluate the performance of different algorithms and verify the robustness of the model to varying noise levels. In the simulation experiment, the Poisson noise photon number was 5×10^6 and the mean and standard deviation of the Gaussian white noise were zero and 1% of the maximum projection data, respectively.

The relaxation factor α was set to 0.25 for SART, PICCS and POCS-TVM (here after abbreviated as TV for convenience). Parameters for the proposed algorithm were $\rho = 0.8$, $\tau = 1$, $\mu = 0.1$, and $\lambda = 0.01$. The maximum number of iterations was 1500 for all reconstruction algorithms.

Reconstruction results using each algorithm, with scanning ranges of [0, 80°], [0, 100°], and [0, 120°], are shown in Fig. 7. The columns show reconstructed results from FBP, SART, TV, PICCS, and the proposed algorithm. A red arrow is included in each mage to indicate the region of interest (ROI). It is evident that reconstructed image quality deteriorates with decreased scanning range. Limited-angle artifacts and edge distortion are also more obvious in the FBP reconstructions. The SART images include a fair amount of noise artifacts and feature distortion. In contrast, images reconstructed by TV, PICCS, and the proposed algorithm are mostly free of noise. However, minor distortions are visible in the enlarged red rectangles of ROI1 and ROI2 for images reconstructed using TV and PICCS algorithm, at scanning

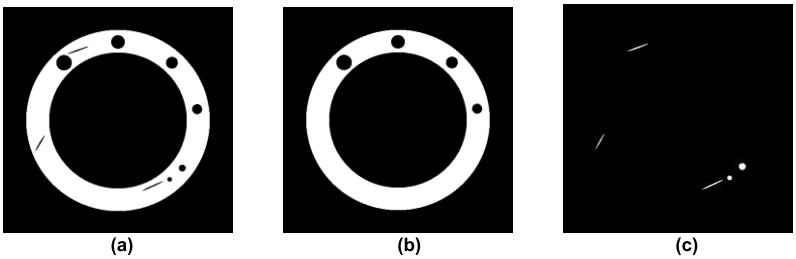

FIGURE 6. The (a) phantom, (b) prior image, and (c) absolute value of the difference between the phantom and the prior image.

TABLE 1. Geometric scanning parameters of simulated CT system.

Distance between source and object center	800 mm
Distance between object center and detector center	102.4 mm
Angle interval of two adjacent projection views	1°
Detector numbers	512
Detector unit	0.4 mm
Pixel size	0.35 mm
Image size	512×512

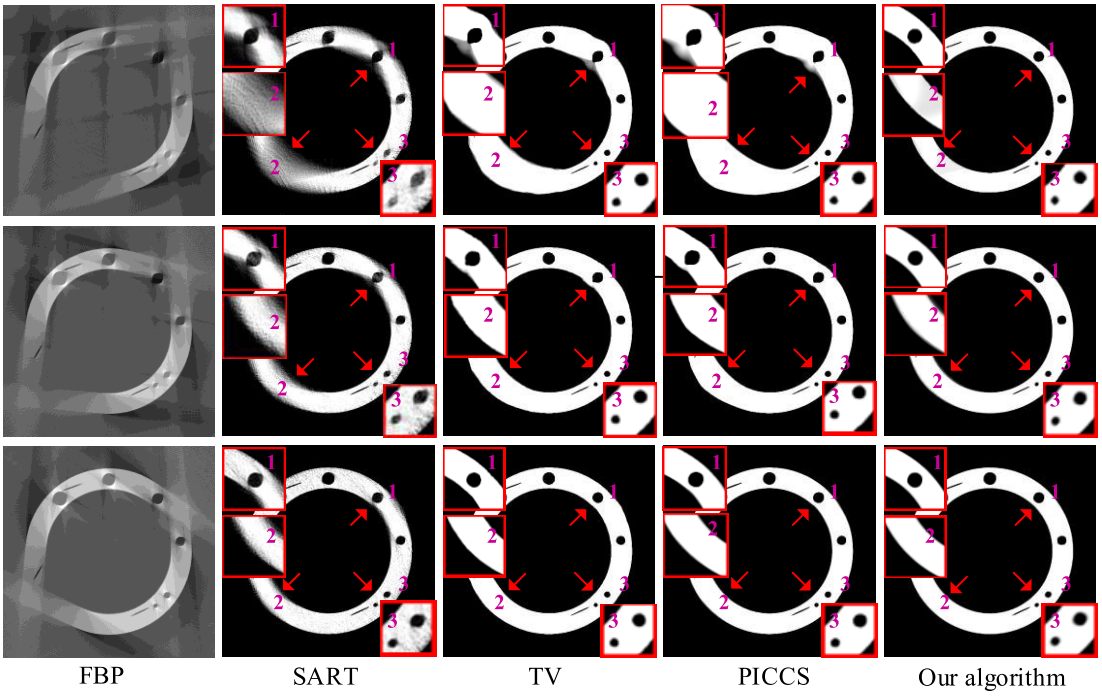

FIGURE 7. Reconstructed results from the simulation phantom for different scanning ranges using the FBP, SART, TV, PICCS, and proposed algorithms. Scanning ranges in the first, second, and third rows were [0, 80°], [0, 100°], and [0, 120°], respectively. The scanning range in the lower left was [0, 360°]. The display window was [0.2, 0.8]. The Poisson noise quantum number was 5×10^6, and the standard deviation of the Gaussian white noise was 1% of the maximum projection data.

ranges of [0, 80°] and [0, 100°]. These distortions did not occur in images reconstructed using the proposed algorithm, which used prior images to preserve edges. In addition, critical information not included in the prior image (i.e., two small porosities and three cracks) were reconstructed by our algorithm. This analysis suggests the proposed technique not only suppresses limited-angle artifacts and preserves edges, but also retains information not included in the prior image.

Quantitative results for the reconstructed images are provided in Table. 2. As shown, compared with the SART, TV, and PICCS algorithms, our technique achieved a lower RMSE and higher MSSIM and PSNR values than SART, TV, or PICCS, even at high noise levels. Fig. 8 demonstrates algorithm convergence by plotting MSSIM, PSNR, and RMSE as a function of iteration number for different scanning ranges. Columns in the figure correspond to scann-ing ranges of

TABLE 2. Quantitative results for different algorithms at varying scanning ranges.

Scanning ranges	Algorithm	MSSIM	PSNR	RMSE
0-80°	SART	0.9676	28.8820	0.0220
	TV	0.9775	29.0343	0.0208
	PICCS	0.9835	29.3049	0.0201
	Our algorithm	0.9884	29.4965	0.0189
0-100°	SART	0.9777	29.5089	0.0203
	TV	0.9826	29.7420	0.0187
	PICCS	0.9861	30.1697	0.0181
	Our algorithm	0.9894	30.2981	0.0176
0-120°	SART	0.9891	31.4521	0.0185
	TV	0.9932	31.8941	0.0182
	PICCS	0.9948	32.1207	0.0179
	Our algorithm	0.9973	32.2848	0.0173

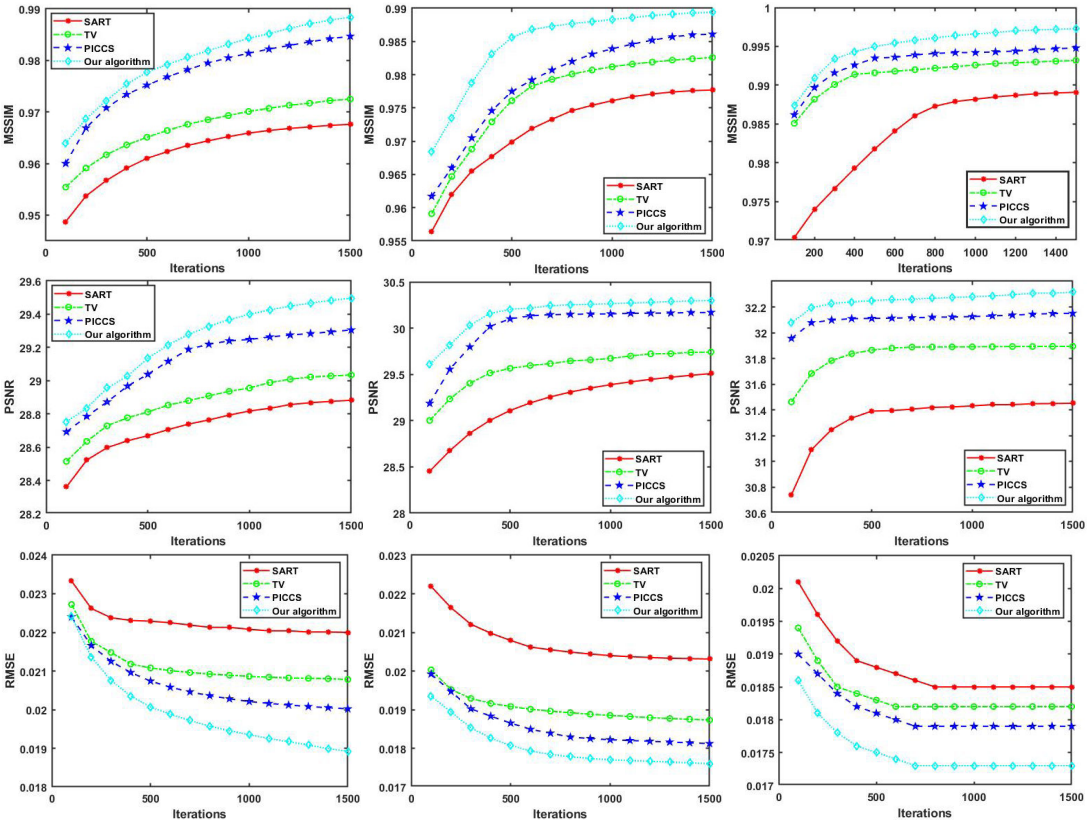

FIGURE 8. Convergence curves for the different algorithms at various scanning ranges. The first, second, and third columns display MSSIM, PSNR, and RMSE results with varying iteration quantities for scanning ranges of [0, 80°], [0, 100°], and [0, 120°].

[0, 80°], [0, 100°], and [0, 120°]. It is evident the proposed algorithm achieved the fastest convergence.

Finally, compared with the $\tau NLR((WX)_L)$ term, we considered the $\tau \|(WX)_L\|_0$ term in the model (17), and the hard thresholding method was used to solve the l_0 minimization sub-problem, which was named the "l_2-l_0" algorithm according to the regularization terms. Then, "our algorithm" was named the "l_2-*NLR*" algorithm. We tested the performance of the l_2-l_0 algorithm for limited-angle CT reco-nstruction, and the reconstructed results were compared with the l_2-*NLR* algorithm.

A simulated phantom (see Fig. 6) was utilized to test the performance of the l_2-l_0 algorithm, and the scanning parameters of the simulated limited-angle CT are given in Table 1. The scanning ranges [0, 80°], [0, 100°], and [0, 120°] were investigated, and the number of projection views were 81,101, and 121, respectively. The Poisson noise photon number was 5×10^6, the mean and standard deviation of Ga-ussian white noise were zero and 1% of the maximum projection data, respectively.

The reconstructed results for the different scanning ranges using the l_2-l_0 and l_2-*NLR* algorithms are shown in Fig. 9. The first, second, and third columns are the recon- structed results for the scanning ranges [0, 80°], [0, 100°], and [0, 120°], respectively. From top to bottom, Fig. 9 sho-ws the reconstructed results using the l_2-l_0 and l_2-*NLR* algo-rithms

TABLE 3. Quantitative results for different algorithms at varying scanning ranges.

Scanning ranges	Algorithm	MSSIM	PSNR	RMSE
0-80°	l_2-l_0	0.9792	29.0547	0.0204
	l_2-*NLR*	0.9884	29.4965	0.0184
0-100°	l_2-l_0	0.9826	29.1937	0.0189
	l_2-*NLR*	0.9894	30.2981	0.0181
0-120°	l_2-l_0	0.9934	32.0983	0.0178
	l_2-*NLR*	0.9975	32.2851	0.0175

TABLE 4. Geometric scanning parameters for the practical CT system.

Distance between source and object center	1060 mm
Distance between object center and detector center	140 mm
Angle interval for two adjacent projection views	1°
Detector numbers	1536
Detector unit	0.127 mm
Pixel size	0.3354 mm
Image size	512×512

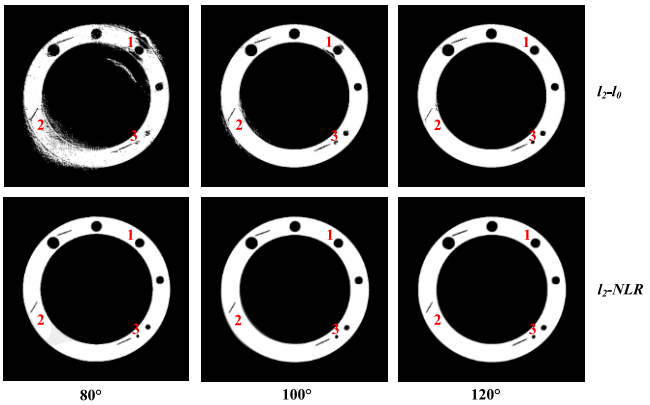

FIGURE 9. Reconstructed results from the simulation phantom for different scanning ranges using the l_2 - l_0 and l_2 -*NLR* algorithms. Scanning ranges in the first, second, and third columns were [0, 80°], [0, 100°], and [0, 120°], respectively. The display window was [0.37, 0.59].

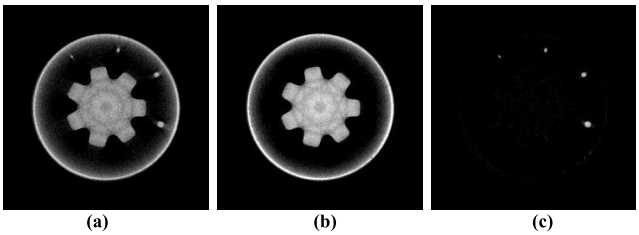

FIGURE 10. (a) The reconstructed image of the motor mock-up with porosity, using the FBP algorithm with a scanning range of [0, 360°]. Also shown are (b) the prior image without porosity and (c) the absolute value of the difference between (a) and (b). The display window is [0.1, 1.0].

in each row. As shown in Fig. 9, the limited-angle artifacts were better suppressed and the edges of the re-constructed images were better preserved using the l_2-*NLR* algorithm for limited-angle reconstruction problems. However, some noise is visible in the ROI1, ROI2, and ROI3 for images reconstructed using the l_2-l_0 algorithm, at scanning ranges of [0, 80°] and [0, 100°]. The reconstruction quality is characterized quantitatively in Table. 3. As shown in Table 3, compared with the l_2-l_0 algorithms, our algorithm achieved a lower RMSE and higher MSSIM and PSNR values, even at high noise levels.

B. EXPERIMENT WITH PRACTICAL DATA

The viability of the proposed algorithm for limited-angle reconstructions was further validated using actual CT data from a motor mock-up. Scanning parameters for this practical limited-angle CT system are provided in Table. 4. Scanning ranges of [0, 120°], [0, 100°], and [0, 80°] were investigated with 121, 101, and 81 projections, respectively. The reconstructed image of the motor mock-up (with porosi-ty) and the prior image (without porosity), used in both the PICCS algorithm and our algorithm, are shown in Fig. 10.

In this set of experiments, the relaxation factor α was set to 0.28 for the SART, TV, and PICCS algorithms. Parameters for the proposed technique were $\rho = 0.8$, $\tau = 1$, $\mu = 0.1$, and $\lambda = 0.01$. The maximum number of iterations in the outer loop of all reconstruction algorithms was 2000.

Reconstruction results for the five algorithms using actual projection data with different scanning ranges, are shown in Fig. 11. The ROI is labelled by a red rectangle and a red arrow. As shown in Fig.11, the slope artifacts in the results reconstructed using PICCS and our algorithm, can be suppressed further. The edges labelled by red arrow 1 and red arrow 2 could also be better preserved in the limited-angle problem. The enlarged ROI in Fig. 11, labelled by the red rectangle, demonstrates that noise suppression in the images reconstructed using our technique is superior to that of the PICCS, TV, or SART algorithms. The four porosities, which were not included in the prior image, could also be reconstructed more accurately from limited-angle projection data. However, some nonuniformity is presented in the inner part of the images shown in Fig. 11, as the scanning range increases. The reason is that these five algorithms are sensitive to ring artifacts which are caused by inconsistent pixel response of the flat panel detector.

We considered the image reconstructed using the FBP algorithm, with a scanning range of [0, 360°], to be the reference image. Quantitative results for the reconstructions are provided in Table. 5. As shown, the proposed algorithm achieved a lower RMSE and higher MSSIM and PSNR values

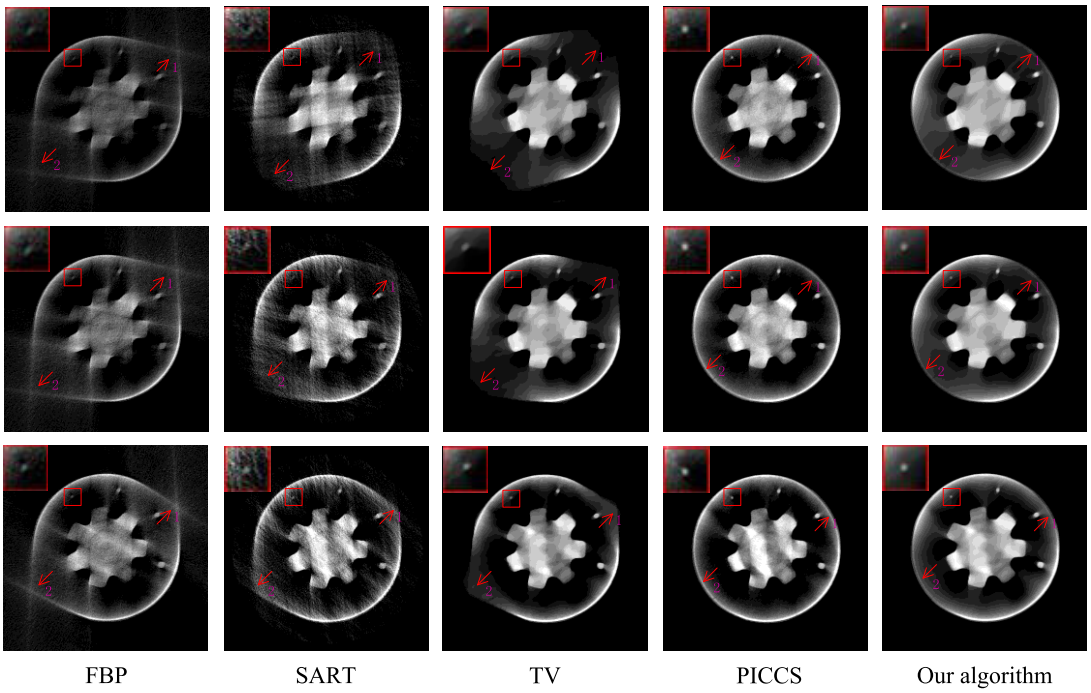

FIGURE 11. Reconstructed images of the motor mock-up for different scanning ranges, using the FBP, SART, TV, PICCS, and proposed algorithm. Scanning ranges in the first, second, and third rows were [0, 80°], [0, 100°], and [0, 120°], respectively. The ROI is labelled by the red rectangle and the red arrow. The display window is [0.4, 1.4].

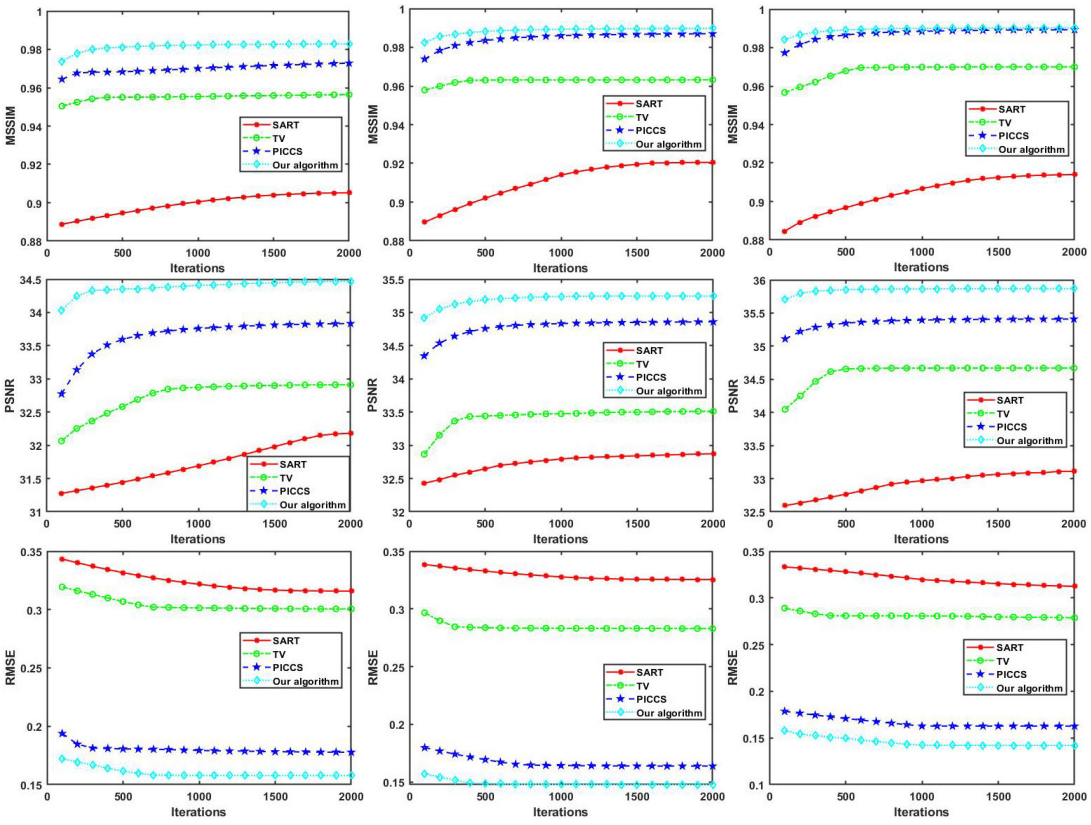

FIGURE 12. Convergence curves for the different algorithms at various scanning ranges. The first, second, and third columns display MSSIM, PSNR, and RMSE results, respectively, with varying iteration quantities for scanning ranges of [0, 80°], [0, 100°], and [0, 120°].

TABLE 5. Quantitative results for varying algorithms and scanning ranges.

Scanning ranges	Algorithm	MSSIM	PSNR	RMSE
0-80°	SART	0.9052	32.1808	0.3158
	TV	0.9564	32.9118	0.3006
	PICCS	0.9728	33.8331	0.1777
	Our algorithm	0.9828	34.4669	0.1578
0-100°	SART	0.9205	32.8719	0.3155
	TV	0.9632	33.5118	0.2830
	PICCS	0.9870	34.8587	0.1638
	Our algorithm	0.9898	35.2462	0.1478
0-120°	SART	0.9140	33.1112	0.3124
	TV	0.9700	34.6690	0.2787
	PICCS	0.9893	35.4088	0.1626
	Our algorithm	0.9903	35.8683	0.1419

than SART, TV, or PICCS. Fig. 12 demonstrates algorithm convergence by plotting MSSIM, PSNR, and RMSE as a function of iteration number for different scanning ranges. Columns in the figure correspond to scanning ranges of [0, 80°], [0, 100°], and [0, 120°]. It is evident that the proposed algorithm achieved the fastest convergence.

V. CONCLUSION

In this study, a minimization model based on nonlocal low-rank and prior images under a wavelet framework was proposed to suppress limited-angle artifacts in CT reconstructions. In addition, ADMM was included to provide an alternative and effective solution to the minimization problem. Experimental results showed our algorithm can suppress limited-angle artifacts in the reconstructed images, effectively recover edge information, and produce high-quality reconstructed images from limited-angle data. In addition, critical information not included in the prior image was preserved. As shown in Fig. 8 and Fig. 12, the proposed algorithm also achieved faster convergence. These experiments only included fan-beam limited-angle CT projections, and the parameters and the number of iterations were selected by trial and error. In the future, we plan to study other applications of our model and address the optimization of imaging parameters.

REFERENCES

[1] L. Li, K. Kang, Z. Chen, L. Zhang, Y. Xing, H. Yu, and G. Wang, "An alternative derivation and description of Smith's data sufficiency condition for exact cone-beam reconstruction," *J. X-Ray Sci. Technol.*, vol. 16, no. 1, pp. 43–49, Jan. 2008, doi: 10.1109/TGRS.2008.2002323.

[2] H. K. Tuy, "An inversion formula for cone-beam reconstruction," *SIAM J. Appl. Math.*, vol. 43, no. 3, pp. 546–552, Jun. 1983.

[3] H. Gao, "Volumetric imaging from a multisegment straight-line trajectory and a practical reconstruction algorithm," *Opt. Eng.*, vol. 46, no. 7, Jul. 2007, Art. no. 077004, doi: 10.1117/1.2756823.

[4] Z. Wang, Z. Huang, Z. Chen, L. Zhang, X. Jiang, X. Kang, H. Yin, H. Wang, and M. Stampanoni, "Low-dose multiple-information retrieval algorithm for X-ray grating-based imaging," *Nucl. Instrum. Methods Phys. Res. A, Accel. Spectrom. Detect. Assoc. Equip.*, vol. 635, no. 1, pp. 103–107, Apr. 2011, doi: 10.1016/j.nima.2011.01.079.

[5] L. Li, Z. Chen, L. Zhang, and K. Kang, "An exact reconstruction algorithm in variable pitch helical cone-beam CT when PI-line exists," *J. X-Ray Sci. Technol.*, vol. 14, no. 2, pp. 109–118, Jan. 2006.

[6] L. Li, Z. Chen, K. Kang, L. Zhang, and Y. Xing, "Recent advance in exact ROI/VOI image reconstruction," *Current Med. Imag. Rev.*, vol. 6, no. 2, pp. 112–118, May 2010, doi: 10.2174/157340510791268506.

[7] G. L. Zeng, "Image reconstruction—A tutorial," *Comput. Med. Imag. Grap.*, vol. 25, no. 2, pp. 97–103. Mar. 2001, doi: 10.1016/S0895-6111(00)00059-8.

[8] R. Gordon, R. Bender, and G. T. Herman, "Algebraic reconstruction techniques (ART) for three-dimensional electron microscopy and X-ray photography," *J. Theor. Biol.*, vol. 29, no. 3, pp. 471–481, Dec. 1970, doi: 10.1016/0022-5193(70)90109-8.

[9] A. H. Andersen and A. C. Kak, "Simultaneous algebraic reconstruction technique (SART): A superior implementation of the art algorithm," *Ultrason. Imag.*, vol. 6., pp. 94–181. Feb. 1984, doi: 10.1016/0161-7346(84)90008-7.

[10] K. Lange and R. Carson, "EM reconstruction algorithms for emission and transmission tomography," *J. Comput. Assist. Tomogr.*, vol. 8, no. 2, pp. 306–316, Apr. 1984, doi: 10.1097/00004728-198404000-00002.

[11] J. M. Fadili and G. Peyré, "Total variation projection with first order schemes," *IEEE Trans. Image Process.*, vol. 20, no. 3, pp. 657–669, Mar. 2011, doi: 10.1109/TIP.2010.2072512.

[12] J. Heide Jørgensen, T. Lindstrøm Jensen, P. Christian Hansen, S. Holdt Jensen, E. Y. Sidky, and X. Pan, "Accelerated gradient methods for total-variation-based CT image reconstruction," 2011, *arXiv:1105.4002*. [Online]. Available: http://arxiv.org/abs/1105.4002

[13] Z. Tian, X. Jia, K. Yuan, T. Pan, and S. B. Jiang, "Low-dose CT reconstruction via edge-preserving total variation regularization," *Phys. Med. Biol.*, vol. 56, no. 18, pp. 5949–5967, Sep. 2011, doi: 10.1088/0031-9155/56/18/011.

[14] E. Y. Sidky, C.-M. Kao, and X. Pan, "Accurate image reconstruction from few-views and limited-angle data in divergent-beam CT," *J. X-Ray Sci. Technol.*, vol. 14, no. 2, pp. 119–139, May 2009, doi: 10.1364/JOSAA.25.001772.

[15] Z. Chen, X. Jin, L. Li, and G. Wang, "A limited-angle CT reconstruction method based on anisotropic TV minimization," *Phys. Med. Biol.*, vol. 58, no. 7, pp. 2119–2141, Mar. 2013, doi: 10.1088/0031-9155/58/7/2119.

[16] L. Zeng, J. Guo, and B. Liu, "Limited-angle cone-beam computed tomography image reconstruction by total variation minimization and piecewise-constant modification," *J. Inverse Ill-Posed Problems*, vol. 21, no. 6, pp. 735–754, Jan. 2013, doi: 10.1515/jip-2011-0010.

[17] X. Lu, Y. Sun, and Y. Yuan, "Image reconstruction by an alternating minimisation," *Neurocomputing*, vol. 74, no. 5, pp. 661–670, Feb. 2011, doi: 10.1016/j.neucom.2010.08.003.

[18] X. Lu, Y. Sun, and Y. Yuan, "Optimization for limited angle tomography in medical image processing," *Phys. Med. Biol.*, vol. 44, p. 24 27-2435. Dec. 2011, doi: 10.1016/j.patcog.2010.12.016.

[19] G. T. Herman and R. Davidi, "Image reconstruction from a small number of projections," *Inverse Problems*, vol. 24, no. 4, pp. 45011–45028, Aug. 2008, doi: 10.1088/0266-5611/24/4/045011.

[20] N. K. Kumar and J. Schneider, "Literature survey on low rank approximation of matrices," *Linear Multilinear Algebra*, vol. 65, no. 11, pp. 2212–2244, Jun. 2016, doi: 10.1080/03081087.2016.1267104.

[21] W. Dong, G. Shi, X. Li, Y. Ma, and F. Huang, "Compressive sensing via nonlocal low-rank regularization," *IEEE Trans. Image Process.*, vol. 23, no. 8, pp. 3618–3632, Aug. 2014, doi: 10.1109/TIP.2014.2329449.

[22] S. V. Mohd Sagheer and S. N. George, "Denoising of low-dose CT images via low-rank tensor modeling and total variation regularization," *Artif. Intell. Med.*, vol. 94, pp. 1–17, Mar. 2019, doi: 10.1016/j.artmed.2018.12.006.

[23] X. Jia, B. Dong, Y. Lou, and S. B. jiang, "GPU-based iterative cone-beam CT reconstructionusing tight frame regularization," *Phys. Med. Biol.*, vol. 56, no. 13, pp. 3787–3806, May 2010, doi: 10.1088/003-9155/56/13/0.04.
[24] W. Zhou, J.-F. Cai, and H. Gao, "Adaptive tight frame based medical image reconstruction: A proof-of-concept study for computed tomography," *Inverse Problems*, vol. 29, no. 12, pp. 1–18, Nov. 2013, doi: 10.1088/0266-5611/29/12/125006.
[25] B. Zhao, H. Gao, H. Ding, and S. Molloi, "Tight-frame based iterative image reconstruction for spectral breast CT," *Med. Phys.*, vol. 40, no. 3, Mar. 2013, Art. no. 031905, doi: 10.1118/1.4790468.
[26] H. Kong, L. Lei, and P. Chen, "Spectral CT reconstruction algorithm based on adaptive tight frame wavelet and total variation," in *Proc. SPIE*, Philadelphia, PA, USA, 2019, pp. 1–7, doi: 10.1117/12.2534488.
[27] G. H. Chen, J. Tang, and S. Leng, "Prior image constrained compressed sensing (PICCS): A method to accurately reconstruct dynamic CT images from highly undersampled projection data sets," *Med. Phys.*, vol. 35, no. 2, pp. 660–663, Feb. 2008, doi: 10.1117/12.770532.
[28] G.-H. Chen, J. Tang, and J. Hsieh, "Temporal resolution improvement using PICCS in MDCT cardiac imaging," *Med. Phys.*, vol. 36, no. 6, pp. 2130–2135, Jun. 2009, doi: 10.1118/1.3130018.
[29] J. Tang, J. Hsieh, and G.-H. Chen, "Performance study of the temporal resolution improvement using prior image constrained compressed sensing (TRI-PICCS)," *Proc. SPIE Med. Imag., Phys. Med. Imag.*, vol. 7622, Mar. 2010, Art. no. 762222, doi: 10.1117/12.844537.
[30] B. Nett, J. Tang, B. Aagaard-Kienitz, H. Rowley, and G. Chen, "Low radiation dose C-arm cone-beam CT based on prior image constrained compressed sensing (PICCS): Including compensation for image vol. mismatch, between multiple acquisitions," *Proc. SPIE Med. Imag.*, vol. 7258, Mar. 2009, Art. no. 725803, doi: 10.1117/12.813800.
[31] M. G. Lubner, P. J. Pickhardt, D. H. Kim, J. Tang, A. M. del Rio, and G.-H. Chen, "Prospective evaluation of prior image constrained compressed sensing (PICCS) algorithm in abdominal CT: A comparison of reduced dose with standard dose imaging," *Abdominal Imag.*, vol. 40, no. 1, pp. 207–221, Jan. 2015, doi: 10.1007/s00261-014-0178-x.
[32] J. Tang, J. Hsieh, and G.-H. Chen, "Temporal resolution improvement in cardiac CT using PICCS (TRI-PICCS): Performance studies," *Med. Phys.*, vol. 37, no. 8, pp. 4377–4388, Aug. 2010, doi: 10.1118/1.3460318.
[33] S. Boyd, "Distributed optimization and statistical learning via the alternating direction method of multipliers," *Found. Trends Mach. Learn.*, vol. 3, no. 1, pp. 1–122, 2010, doi: 10.1561/2200000016.
[34] A. Ron and Z. Shen, "Affine Systems in L2 (Rd): The Analysis of the Analysis Operator," *J. Funct. Anal.*, vol. 148, no. 2, pp. 408–447. 1997, doi: 10.21236/ada305184.
[35] Ü. Lepik and H. Hein, *Haar Wavelets*. Cham, Switzerland: Springer, 2014, pp. 7–20.
[36] J. Mairal, F. Bach, J. Ponce, G. Sapiro, and A. Zisserman, "Non-local sparse models for image restoration," in *Proc. IEEE 12th Int. Conf. Comput. Vis.*, Oct. 2009, pp. 2272–2279, doi: 10.1109/ICCV.2009.5459452.
[37] M. Fazel, H. Hindi, and S. P. Boyd, "Log-det heuristic for matrix rank minimization with applications to hankel and Euclidean distance matrices," in *Proc. Amer. Control Conf.*, Denver, CO, USA, Nov. 2003, pp. 2156–2162, doi: 10.1109/ACC.2003.1243393.
[38] W. Huabin, L. Cheng, and Z. Jian, "Orthogonal projection non-negative matrix factorization using alternating direction method of multipliers," *J. Image Graph.*, vol. 22, no. 4, pp. 463–471. Apr. 2017, doi: 10.11834/jig.20170406.
[39] Y. Zhang, B. Dong, and Z. Lu, "ℓ_0 minimization for wavelet frame based image restoration," *Math. Comput.*, vol. 82, no. 282, pp. 995–1015, Apr. 2013, doi: 10.1090/S0025-5718-2012-02631-7.
[40] M. Storath, A. Weinmann, J. Frikel, and M. Unser, "Joint image reconstruction and segmentation using the Potts model," *Inverse Problems*, vol. 31, no. 2, p. 025003, 2015, doi: 10.1088/02665611/31/2/025003.
[41] Z. Wang, A. C. Bovik, H. R. Sheikh, and E. P. Simoncelli, "Image quality assessment: From error visibility to structural similarity," *IEEE Trans. Image Process.*, vol. 13, no. 4, pp. 600–612, Apr. 2004, doi: 10.1109/tip.2003.819861.
[42] J. Xu and B. M. W. Tsui, "Electronic noise modeling in statistical iterative reconstruction," *IEEE Trans. Image Process.*, vol. 18, no. 6, pp. 1228–1238, Jun. 2009, doi: 10.1109/TIP.2009.2017139.
[43] J. Ma, Z. Liang, Y. Fan, Y. Liu, J. Huang, W. Chen, and H. Lu, "Variance analysis of X-ray CT sinograms in the presence of electronic noise background," *Med. Phys.*, vol. 39, no. 7Part1, pp. 4051–4065, Jun. 2012, doi: 10.1118/1.4722751.

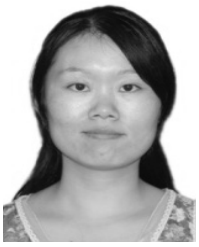

NA XU received the bachelor's degree in electronic information science and technology from the Baoji University of Arts and Sciences, Baoji, Shanxi, China, in 2009, and the master's degree in engineering from Chongqing University, Chongqing, China, in 2013. She is currently pursuing the Ph.D. degree with the North University of China, Taiyuan, Shanxi, China. She is also a Lecturer with the Department of Electronic Information Engineering, Shanxi University, Taiyuan. She has been with the university for the past seven years. Her research interests include motion video processing and computed tomography (CT) image reconstruction.

HUILING HOU was born in 1981. She received the Ph.D. degree from the North University of China, China, in 2015. She is currently an Associate Professor with the North University of China. Her research interests include image processing and computed tomography (CT) image reconstruction.

ZHIYONG CHENG received the B.Sc. degree. He is currently pursuing the master's degree in electronics and communication engineering with the North University of China. His current research interests include image processing and computed tomography (CT) image reconstruction.

MINGQUAN WANG was born in 1970. He received the Ph.D. degree from the North University of China, Taiyuan, Shanxi, China, in 2004. He is currently a Professor with the North University of China. His research interests include image processing and reconstruction, and X-ray detection.

YU WANG received the Ph.D. degree from the College of Information and Communication Technology, North University of China, in 2014. Since 2014, she has been an Associate Professor with the North University of China. Her research interests include medical image segmentation, medical image registration, and artificial intelligence.

GUOGANG WANG was born in Taian, Shandong, China, in 1977. He received the B.S. degree in applied mathematics from Qufu Normal University, Qufu, Shandong, China, in 2000, and the M.S. degree in applied mathematics and the Ph.D. degree in signal and information processing from the Nanjing University of Posts and Telecommunications, Nanjing, Jiangsu, China, in 2011 and 2016, respectively. He is currently an Associate Professor with Shanxi University. His research interests include computer vision, image processing, and pattern recognition.